Applied Catalysis B: Environmental 168-169 (2015) 572–576

Contents lists available at ScienceDirect

Applied Catalysis B: Environmental

journal homepage: www.elsevier.com/locate/apcatb

Improving photocatalytic hydrogen production of metal–organic framework UiO-66 octahedrons by dye-sensitization

Yu-Peng Yuan[a,b], Li-Sha Yin[b], Shao-Wen Cao[b], Geng-Sheng Xu[a], Chuan-Hao Li[a,*], Can Xue[b,*]

[a] Laboratory of Advanced Porous Materials, School of Chemistry and Chemical Engineering, Anhui University, Hefei 230036, PR China
[b] Solar Fuels Lab, School of Materials Science and Engineering, Nanyang Technological University, 50 Nanyang Avenue, Singapore 639798, Singapore

ARTICLE INFO

Article history:
Received 27 August 2014
Received in revised form 1 November 2014
Accepted 3 November 2014
Available online 13 November 2014

Keywords:
Photocatalysis
Water splitting
Dye sensitization
Metal–organic frameworks

ABSTRACT

We used Erythrosin B dye to sensitize Zr-containing MOFs of UiO-66 octahedrons for photocatalytic H_2 production. No H_2 production was observed over Pt-loaded UiO-66 octahedrons under visible light irradiation. Comparatively, efficient hydrogen production was achieved upon visible light irradiation in this dye sensitized MOFs system. The highest H_2 production rate of 4.6 μmol h^{-1}, corresponding to 0.25% quantum efficiency at 420 nm, occurs from the system containing 10 mg MOFs photocatalyst and 30 mg Erythrosin B dye. The enhancement in photocatalytic H_2 production was benefited from the efficient charge transfer from photoexcited Erythrosin B dye to the MOFs. Owing to the advantages of low cost, easy operation, and abundance in nature, the dye sensitized MOFs shows great potential for photocatalytic H_2 production.

1. Introduction

As a clean energy source, hydrogen fuel has attracted tremendous efforts because of its high energy density. Photocatalytic water splitting has been considered as a promising technique for hydrogen production because it allows the conversion of clean, safe, and renewable solar energy to chemical fuels [1–4]. Over 100 inorganic semiconductor photocatalysts are demonstrated to generate hydrogen fuels [5]. These include titanium dioxide (TiO_2) [6], cadmium sulfide (CdS) [7], $In_{1-x}Ni_xTaO_4$ [8], $NaTaO_3$ [9], $(Ga_{1-x}Zn_x)(N_{1-x}O_x)$ [10], and g-C_3N_4 [11], etc. However, the conversion efficiency of the current materials is still very low, which is caused by the weak light absorption ability, narrow photoresponse, rapid recombination, and poor photostability. Thus it is still an essential challenge to develop new efficient photocatalysts for hydrogen production.

Recently metal–organic frameworks (MOFs) have emerged as potential promising candidates for photocatalytic reactions [12,13]. MOFs are crystalline compounds in which the metal or metal clusters are cross-linked by polyfunctional organic linkers. Similar to conventional inorganic photocatalysts, such as metal oxides and sulfides, in which the metal ions are cross-linked by O^{2-} and S^{2-} ions, organic linkers in MOFs act as the "function" of O^{2-} and S^{2-} ions in conventional photocatalysts. From the viewpoint of crystal structure, MOFs can therefore behavior as semiconductors, in which the conduction band is composed of the empty outer orbitals of metal centers and the valence band is constructed by the outer orbitals of organic components. Upon light illumination, organic linkers as photon antennas will be excited to generate electrons and holes, which is the essential process for photocatalytic reactions. In addition, MOFs could be synthesized by versatile synthetic strategies including solvothermal, vapor diffusion, emulsion-assistant precipitation, and sonication approaches [14–16] Compared with the conventional photocatalysts, photoactive MOFs exhibit the highly porous structure (with surface area up to 1000 m^2 g^{-1}), which facilitates the mass transport in photocatalytic reactions [17]. Also, the controllable chemical and physical properties could be easily realized by tuning the organic functionalities and metal center at the molecular level. However, MOFs suffered from poor photostability. In 2010, Garcia and co-workers used a highly stable Zr-containing MOFs of UiO-66 and UiO-66(NH_2) for water splitting under UV light irradiation, which opened the door for MOFs to photocatalytic water splitting [18]. To extend the photoresponse of MOFs, a visible-light-absorbing metal complexes or organic building units and catalytically active hydrogen evolution sites (Pt nanoparticles or organometallic compounds) have been

* Corresponding authors at: Laboratory of Advanced Porous Materials, School of Chemistry and Chemical Engineering, Anhui University, Hefei 230036, PR China.
E-mail addresses: lichuanhao1983@163.com, ypyuan@ntu.edu.sg (C.-H. Li), cxue@ntu.edu.sg (C. Xue).

http://dx.doi.org/10.1016/j.apcatb.2014.11.007
0926-3373/

incorporated into the MOFs. For example, Mori and co-workers reported a porous $[Ru_2(p\text{-}BDC)_2]_n$ (BDC = benzenedicarboxylate) MOF for hydrogen production under visible light irradiation, wherein $Ru(bpy)_3^{2+}$, MV^{2+}, and Na_2EDTA were used as photosensitizer, electron relay, and sacrificial reductant, respectively [19]. Lin and co-workers assembled Pt nanoparticle inside the MOFs' channels for active hydrogen production under visible light irradiation [20]. Rosseinsky and co-workers synthesized a water-stable porous Al-containing porphyrin MOF (Al-PMOF) for visible-light-driven hydrogen evolution from water [21]. Xu and co-workers reported a new hydrogen generation system by immobilizing a platinum complex inside the 2,2′-bipyridine-based microporous MOF (MOF-253) [22]. These tentative systems exhibit the low efficiency, high cost, and tedious synthetic processes.

Alternative promising approach to realize efficient visible light photoresponse is to construct dye-sensitized system, which has been widely used in photocatalytic H_2 production [23]. Up to now, several dye-sensitized photocatalysts have also been reported for hydrogen production [24–26]. Given both MOFs and dyes containing benzene ring, it is expected that a strong π–π stacking and Van Der Waals interaction between MOFs and dyes, which is very important for efficient electron transfer in dye-sensitized photocatalyst system [24,25]. In addition, the metal centers separated by organic linkers in MOFs can serve as "quantum dots", therefore the short transport length of charge carriers can be achieved in MOFs. Furthermore, water molecules can easily diffuse into the pores in MOFs, thus making water reduction in MOFs as "quasi-homogeneous reaction". The above-mentioned advantages make MOFs as potential active photocatalysts in water reduction for hydrogen production. Very recently, a Rhodamine B sensitized MOFs was used for water splitting [27]. However, the poor photostability of Rhodamine B dye makes it not suitable as a photosensitizer [28].

Herein, we use low cost Erythrosin B (denoted as ErB) dye as light absorbing antenna and demonstrate an active hydrogen production system over ErB-sensitized Zr-containing MOFs octahedron (UiO-66). ErB dye is a relatively stable organic dye which has been used for durable photocatalytic H_2 production using visible light [25]. Furthermore, UiO-66 as a stable MOF has been reported for photocatalytic hydrogen production and organic conversion [29–31].

2. Experiments

2.1. Synthesis of UiO-66 MOF

All reagents were analytical grade and were used without further purification. UiO-66 photocatalyst was synthesized following a previous synthesis protocol [32]. In a typical synthesis, $ZrCl_4$ (37.3 mg) and 1,4-benzendicarboxylic acid (BDC) (26.6 mg) were first dissolved in 16.34 mL *N*,*N*-dimethylformamide (DMF). Acetic acid (3.66 mL, 3.8 mg) was then added into the solution, following the ultrasonic treatment for 20 min. The homogeneous solution was then transferred into a 40-mL Teflon-lined stainless steel autoclave and heated to 120 °C for 24 h. After cooling to room temperature, the products were collected by centrifugation and wash three times with DMF, and then soaked in methanol at 60 °C for three days with replacing the methanol every 24 h to exchange the DMF solvent.

2.2. Characterizations

X-ray powder diffraction (XRD) data were collected on a Shimadzu XRD-6000 X-ray diffractometer using Cu $K\alpha 1$ radiation at a scan rate of $1^\circ\,min^{-1}$. The acceleration voltage and the applied current were 40 kV and 40 mA, respectively. Morphology of the obtained samples was observed by field emission scanning electron microscopy (SEM: JEOL JSM-7600F) and transmission electron microscopy (TEM: JEOL JEM-2100F). UV–vis diffuse reflectance spectra (DRS) were recorded over the spectral range 320–800 nm on a Lambda 750 UV/vis/NIR spectrophotometer (Perkin Elmer, USA). $BaSO_4$ was used as a reflectance standard. The surface area of the obtained samples was determined by the BET method from N_2 adsorption isotherms at 77 K (ASAP-2020, Micromeritics). The photoluminescence (PL) spectra were obtained on a Shimazu RF-5310PC fluorometer at an excitation wavelength of 450 nm. The Mott–Schottky plot was measured on an electrochemical analyzer (Princeton Applied Research, 2273). The electrolyte is 0.5 M Na_2SO_4 aqueous solution (pH = 6.5). The ac amplitude is 10 mV, and the frequency is 1000 Hz.

2.3. Photocatalytic measurements

Photocatalytic H_2 production reactions were carried out in a 50-mL closed quartz flask reactor, which was sealed with Suba Seal rubber septa (Sigma-Aldrich). Pt is always needed to promote H_2 production in photocatalytic water reduction (so-called co-catalyst). In present work, 0.5 wt% Pt was in-situ pre-photodeposited upon UiO-66 surface through injecting small amount of H_2PtCl_6 solution (61 μL, 0.16 wt%) into the reactor containing 20 vol% methanol solution (denoted as Pt-UiO-66), wherein methanol was used as sacrificial reagent. After 1 h irradiation of full arc light, the suspension was centrifuged and washed with methanol. The obtained Pt-UiO-66 was then used as photocatalyst for hydrogen production. Typically, 10 mg Pt-UiO-66 catalysts and various amount of Erythrosin B dye were suspended in 10 mL aqueous solution of L-ascorbic acid (0.1 M, pH = 4.0). The reactor was purged with argon to drive away the residual air. The photocatalytic hydrogen production was initiated by irradiating the suspension with a 300-W xenon lamp (MAX-302, Asahi Spectra, USA) coupled with a UV cut-off filter ($\lambda > 420$ nm). The gas products were analyzed periodically through a gas chromatograph (GC-7890A, Agilent) with a TCD detector.

The apparent quantum efficiency (QE) was measured at 420 nm by using a band pass filter (half width: 10 nm) under the identical reaction condition for H_2 production. The light power at 420 nm was determined with a power meter (1831-R, Newport), while a photon energy at 420 nm can be calculated through the Plank-Einstein relation $E = h\nu$ to be 4.7×10^{-19} J. Therefore, the number of incident photons from the Xenon lamp can be measured. The QE value can then be calculated by using the following equation.

$$QE = \frac{2 \times \text{the number of evolved hydrogen molecules}}{\text{the number of incident photons}} \times 100\% \quad (1)$$

3. Results and discussion

3.1. Sample characterizations

UiO-66 octahedrons were first synthesized through a solvothermal route [32], followed by in-situ photodeposition of Pt nanoparticles. Then the obtained photocatalyst was sensitized by ErB dye for photocatalytic H_2 production.

The powder X-ray diffraction (XRD) pattern provides crystallinity and phase information for UiO-66 and Pt-UiO-66. As shown in Fig. S1, the narrow diffraction peaks suggest the high crystallinity of the resultant products. All the diffraction peaks can be indexed to UiO-66. No phase change was observed after Pt loading, indicating the excellent photostability of UiO-66 in water (Fig. S1). Pt diffraction peaks cannot be detected owing to the low loading amount.

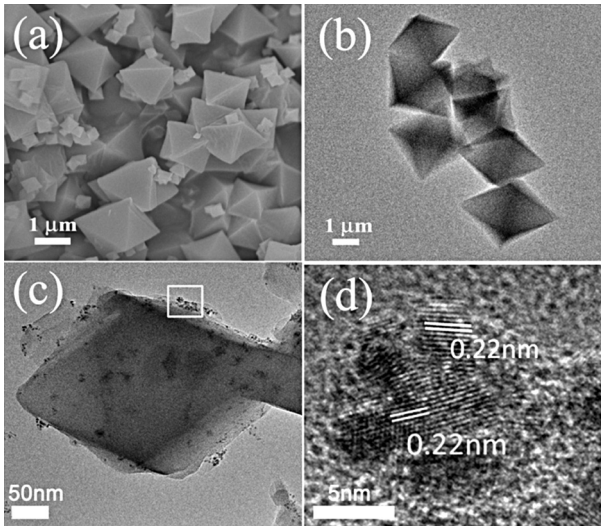

Fig. 1. Micrographs of UiO-66 octahedrons (a) SEM image, (b) TEM image, (c) Pt loaded UiO-66, and (d) HRTEM image of Pt cocatalyst.

Scanning electron microscope (SEM, Fig. 1a) and transmission electron microscope (TEM, Fig. 1b) images show that the products are mainly octahedral microcrystals with an average edge length of ~1 μm. Besides, some small octahedral microcrystals with an average edge length of ~300 nm were also observed. The Pt loading upon UiO-66 surface can be visualized by TEM observation (Fig. 1c). The surface of pristine UiO-66 is very smooth (Fig. 1b), while some small nanoparticles could be observed after Pt loading (Fig. 1c). The energy dispersive X-ray spectroscopy confirmed the presence of Pt (Fig. S2). However, the selected area electron diffraction (SAED) and high-resolution TEM (HRTEM) images of UiO-66 are not attainable owing to the fact that the UiO-66 octahedron tends to be damaged under high energy electron beam irradiation. Fig. 1d presents a typical HRTEM image of the small nanoparticles attached on the surface of Ui-66. The average diameter is about 5 nm. The spacing of the observed lattice fringe is 0.22 nm, which is corresponding to the (1 1 1) crystallographic planes of Pt.

Fig. S3 showsthe N_2 adsorption–desorption isotherm of the prepared UiO-66. It exhibits a typical type-I isotherm with steep increases in N_2 adsorption at a low relative pressure ($P/P_0 < 0.1$), indicating a microporous nature of UiO-66. The measured BET surface area of UiO-66 octahedron is ~982 $m^2\,g^{-1}$. The single point adsorption total pore volume is at $P/P_0 = 0.98$ is 0.49 $cm^3\,g^{-1}$. The highly porous structure will facilitate the photocatalytic reactions. The UV–vis spectrum (Fig. 2a) of the obtained UiO-66 displays an ultraviolet light absorption behaviour with an absorption edge of 350 nm, corresponding to a 3.5 eV band gap (see the inset of Fig. 2a).

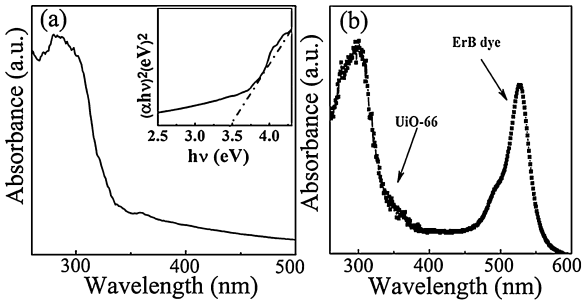

Fig. 2. UV–vis diffraction spectra of (a) UiO-66 octahedrons and (b) suspension of UiO-66 octahedrons and ErB dye.

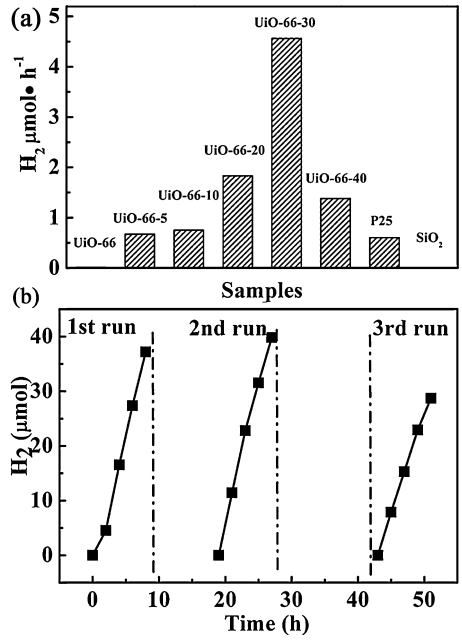

Fig. 3. Photocatalytic H_2 production over the (a) systems with various amount of ErB dye and (b) the recyclability of Pt-UiO-66-30.

The UV–vis spectrum of the suspension shows mixed features of UiO-66 octahedrons and ErB dye (Fig. 2b).

3.2. Photocatalytic H_2 production

To confirm the electron transfer, we evaluated the visible-light-driven (>420 nm) photocatalytic H_2 generation of pristine UiO-66 and ErB dye-sensitized UiO-66. L-ascorbic acid (0.1 M, pH = 4.0) was used as the sacrificial reagent. The As illustrated in Fig. 3a, the pristine Pt-UiO-66 sample shows no activity for H_2 production owing to its non-visible light absorption nature. Also, trance of H_2 evolution was detected from ErB dye suspension (5 mg) with H_2PtCl_6 solution addition. However, upon adding of 5 mg ErB dye (denoted as UiO-66-5, the number 5 indicates the amount of added ErB dye) into the reaction solution, a H_2 evolution rate of ~0.7 μmol h^{-1} was achieved (Fig. 3a and Fig. S4), suggesting the positive sensitization effect of ErB dye on UiO-66 for H_2 production. The photocatalytic H_2 production rate can be further enhanced up to 4.6 μmol h^{-1} by increasing ErB dye amount to 30 mg (Pt-UiO-66-30), which is evidently higher that of ErB dye sensitized P25 and

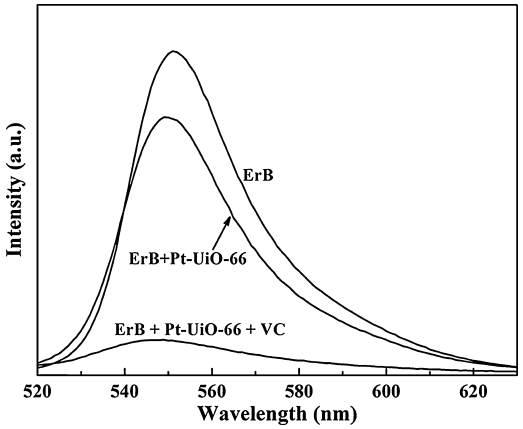

Fig. 4. Steady-state photoluminescence spectra of the ErB dye sensitized UiO-66 system.

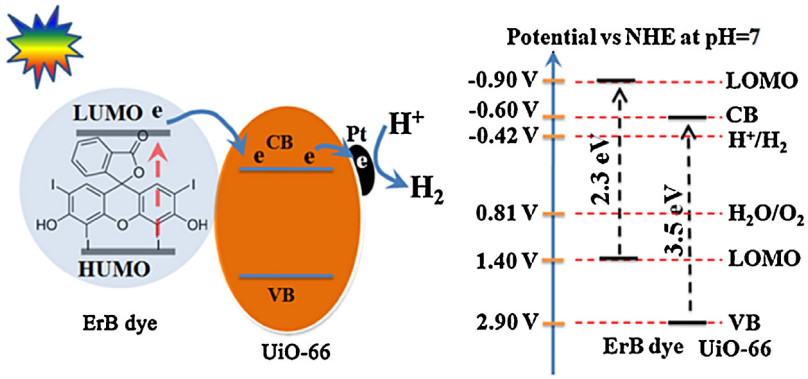

Fig. 5. Suggested charge transfer in ErB dye sensitized UiO-66 for photocatalytic H_2 production and the potential position of ErB dye and UiO-66 MOFs.

SiO_2 under the same experimental condition (Fig. 3a). The higher H_2 production rate of ErB dye sensitized UiO-66 over TiO_2 further demonstrates the priority of MOFs as photocatalysts. In addition, it is worth noting that an induction time at first 2 h in Pt-UiO-66-30 was observed for H_2 production at this system. Comparatively, no induction time for H_2 production was observed in other system (Fig. S4). The reason caused this phenomenon is not yet clear presently. The result suggests that H_2 production rate is heavily dependent on the amount of dyes in reaction system. However, further increasing ErB dye (UiO-66-40) results in a decreased H_2 production rate. The ErB dye absorption over UiO-66 is very weak due to the micropore of UiO-66 (see Fig. S5). Therefore the decrease in H_2 production should be caused by competitive effect that the increase of dynamically non-touched ErB dyes can serve as competitive light-absorbing molecules over touched dyes upon UiO-66 and thereby cause a loss of light harvesting for H_2 production. The photostability of Erythrosin B-sensitized Pt-UiO-66-30 is shown in Fig. 3b. The total amount of H_2 is over 80 μmol after 18 h reactions. The turn over number (TON) is over 300 based on the amount of loaded Pt co-catalyst. After 3 cycles of photoreactions, the hydrogen production activity still retains over 80%, suggesting the excellent photostability of present H_2 generation system. The loss in H_2 production rate is a common problem in dye-sensitization system, which could be caused by the ErB dye consumption or instability of ErB dye under long time visible light irradiation because UiO-66 is very stable in acidic mediate, as evidenced by inductively coupled plasma atomic emission spectrometer (ICP-AES; M6, Thermo Elemental, USA) analysis. Only trace of Zr^{4+} ion was detected by ICP-AES analysis, further confirming the excellent stability of UiO-66 MOF in photocatalytic reactions. Comparatively, the four iodide in ErB dye could be cleaved quickly by light irradiation to low-activity halogen-free analog for photocatalytic H_2 production [33,34]. Therefore, the decreased activity in H_2 production should be caused by the de-halogenation of ErB dye. The quantum efficiency (QE) of the present H_2 production system is measured to be ~0.25% at 420 nm. Note that only 10 mg UiO-66 photocatalyst was used in our experiments for H_2 production. Despite the low QE of the present ErB dye-sensitized UiO-66, the positive effect of dye-sensitization on enhancing the photocatalytic H_2 production of MOFs is still pronounced. More importantly, no changes in morphologies of UiO-66 octahedrons (Fig. S6) was observed after three consecutive usages for H_2 generation, further indicating the excellent stability of the UiO-66 as a new photocatalyst for photocatalytic reactions. Note that the surface of the UiO-66 octahedrons was covered by lots of ErB dyes, confirming the effective attractions between ErB dyes and UiO-66 catalysts caused by the nonbonded π–π stacking and Van Der Waals interactions (Fig. S6).

We also examined the H_2 production rate with various cut-off wavelengths, as shown in Fig. S7. H_2 production rate is essentially determined by the light wavelength. A H_2 production rate of 4.6 μmol h^{-1} was achieved when a 420 nm cut-off filter was equipped. Increased cut-off wavelength causes evident decrease in H_2 production rate. For example, the H_2 production rate decreases to ~1.0 μmol h^{-1} when 470 nm cut-off filter was equipped. Impressively, a H_2 production rate of 0.5 μmol h^{-1} can still achieved when the irradiation light wavelength is longer than 510 nm.

3.3. Mechanism of enhanced photocatalytic H_2 production

To study the photocatalysis mechanism, the steady-state photoluminescence (PL) spectra were measured to monitor the electron transfer from the excited Erythrosin B to UiO-66. As shown in Fig. 4, upon excitation at 450 nm Erythrosin B dye displays a strong emission peak at ~551 nm, which is corresponding to the electrons excitation from the highest occupied molecular orbital (HOMO) of ErB to the lowest unoccupied molecular orbital (LUMO) [25]. After dispersing UiO-66 octahedrons into the Erythrosin B suspension, the intensity of this emission peak shows a significant decrease. Since the UiO-66 does not absorb the visible light, therefore the fluorescence quenching should be caused by the fast electron transfer occurred from the excited ErB to UiO-66 octahedron and thus suppressed the recombination process of photoexcited electron-hole pairs. To verify this assumption, we measured the potential position of UiO-66 by using Mott-Schottky plots (Fig. S8). UiO-66 shows an n-type semiconductor feature, as revealed by the positive slope of the plot. The flat band position is ~0.6 V vs SCE (~0.4 V vs NHE). The conduction band bottom of *n*-type semiconductor is ~0.2 eV above the flat band [35]. Therefore, the conduction band of UiO-66 is estimated to be ~0.6 V vs NHE, which is negative to the redox potential of H^+/H_2 (~0.42 V vs NHE at pH = 7). Meanwhile, the LUMO potential of ErB is ~0.9 V vs NHE [25]. Thus, the electron transfer is thermodynamically favourable from the photoexcited ErB dye to the UIO-66, and then to the Pt active sites for H_2 production, as illustrated in Fig. 5.

This rapid charge transfer process should be arisen from the effective collision between ErB and UiO-66. Notably, this emission peak slightly red shifted from 552 to 549 nm. This small blue-shift in emission peak should be caused by the noncovalent π–π stacking and Van Der Waals interactions of the benzene rings in ErB and UiO-6, which is very similar to the interactions occurred in the system containing g-C_3N_4/graphene and dye molecules [24,25]. As stated above, this noncovalent π–π stacking and Van Der Waals interactions are very critical to host ErB dye molecules onto the UiO-66 and thus facilitates the efficient charge transfer from excited Erythrosin B dyes to UiO-66 under visible light irradiation, thus resulting in the fluorescence quenching. The above results clearly demonstrate that the contact of ErB dye molecules and Pt-UiO-66 plays an essential role on enhancing photocatalytic H_2 evolution. With the increase

of ErB dye added, the amount of adsorbed dye molecules on UiO-66 surface increases, which enhances the antenna effect and leads to the improved H_2 production activity.

4. Conclusions

Erythrosin B was successfully used as a sensitizer to extend the photoresponse of Zr-containing based MOF (UiO-66 octahedrons) into visible light region. A significant improved hydrogen production activity was realized. Given the low cost and easy operation of present H_2 production system, this study provides a potential approach to develop highly efficient MOF-based photocatalysts for hydrogen production.

Acknowledgements

This work was supported by NTU Start-Up Grant (SUG), NTU seed funding for Solar Fuels Laboratory, MOE AcRF-Tier1 (RG 44/11), MOE AcRF-Tier2 (MOE2012-T2-2-041, ARC 5/13), and CRP (NRF-CRP5-2009-04) from NRF Singapore. Y. P. Yuan and C. H. Li acknowledge the support from the National Natural Science Foundation of China (51002001, 21303002), the Research Fund for the Doctoral Program of Higher Education of China (20123401120004) and the State "211 Project" of Anhui University, China.

Appendix A. Supplementary data

Supplementary data associated with this article can be found, in the online version, at http://dx.doi.org/10.1016/j.apcatb.2014.11.007.

References

[1] A. Fujishima, K. Honda, Nature 238 (1972) 37–38.
[2] X.B. Chen, S.H. Shen, L.J. Guo, S.S. Mao, Chem. Rev. 110 (2010) 6503–6570.
[3] Z.J. Han, F. Qiu, R. Eisenberg, P.L. Holland, T.D. Krauss, Science 338 (2012) 1321–1324.
[4] K. Maeda, K. Domen, J. Phys. Chem. C 111 (2007) 7851–7861.
[5] F.E. Osterloh, Chem. Mater. 20 (2008) 35–54.
[6] G. Liu, L.Z. Wang, H.G. Yang, H.M. Cheng, G.Q. Lu, J. Mater. Chem. 20 (2010) 831–843.
[7] X. Zong, H.J. Yan, G.P. Wu, G.J. Ma, F.Y. Wen, L. Wang, C. Li, J. Am. Chem. Soc. 130 (2008) 7176–7177.
[8] Z.G. Zou, J.H. Ye, K. Sayama, H. Arakawa, Nature 414 (2001) 625–627.
[9] H. Kato, K. Asakura, A. Kudo, J. Am. Chem. Soc. 125 (2003) 3082–3089.
[10] K. Maeda, K. Teramura, D.L. Lu, T. Takata, N. Saito, Y. Inoue, K. Domen, Nature 440 (2006) 295.
[11] X.C. Wang, K. Maeda, A. Thomas, K. Takanabe, G. Xin, J.M. Carlsson, K. Domen, M. Antonietti, Nat. Mater. 8 (2009) 76–80.
[12] J.L. Wang, C. Wang, W.B. Lin, ACS Catal. 2 (2012) 2630–2640.
[13] M.A. Nasalevich, M. van der Veen, F. Kapteijn, J. Gascon, Cryst. Eng. Commun. 16 (2014) 4919–4926.
[14] L.J. Murray, M. Dinca, J.R. Long, Chem. Soc. Rev. 38 (2009) 1294–1314.
[15] J.Y. Lee, O.K. Farha, J. Roberts, K.A. Scheidt, S.T. Nguyen, J.T. Hupp, Chem. Soc. Rev. 38 (2009) 1450–1459, http://pubs.rsc.org/en/Content/ArticleLanding/2009/CS/B807080F.
[16] J.R. Li, R.J. Kuppler, H.C. Zhou, Chem. Soc. Rev. 38 (2009) 1477–1504.
[17] W.T. Xu, L. Ma, F. Ke, F.M. Peng, G.S. Xu, Y.H. Shen, J.F. Zhu, L.G. Qiu, Y.P. Yuan, Dalton Trans. 43 (2014) 3792–3798.
[18] C.G. Silva, I. Luz, F.X. Llabrés, I. Xamena, A. Corma, H. García, Chem. Eur. J. 16 (2010) 11133–11138.
[19] Y. Kataoka, K. Sato, Y. Miyazaki, K. Masuda, H. Tanaka, S. Naitoand, W. Mori, Energy Environ. Sci. 2 (2009) 397–400.
[20] C. Wang, K.E. deKrafft, W. Lin, J. Am. Chem. Soc. 134 (2012) 7211–7214.
[21] A. Fateeva, P.A. Chater, C.P. Ireland, A.A. Tahir, Y.Z. Khimyak, P.V. Wiper, J.R. Darwent, M.J. Rosseinsky, Angew. Chem. Int. Ed. 51 (2012) 7440–7444.
[22] T.H. Zhou, Y.H. Du, A. Borgna, J.D. Hong, Y.B. Wang, J.Y. Han, W. Zhang, R. Xu, Energy Environ. Sci. 6 (2013) 3229–3234.
[23] W.J. Youngblood, S.H.A. Lee, K. Maeda, T.E. Mallouk, Acc. Chem. Res. 42 (2009) 1966–1973.
[24] S.X. Min, G.X. Lu, J. Phys. Chem. C 116 (2012) 19644–19652.
[25] Y. Wang, J.D. Hong, W. Zhang, R. Xu, Catal. Sci. Technol. 3 (2013) 1703–1711.
[26] S.X. Min, G.X. Lu, J. Phys. Chem. C 115 (2011) 13938–13945.
[27] J. He, J.Q. Wang, Y.J. Chen, J.P. Zhang, D.L. Duan, Y. Wang, Z.Y. Yan, Chem. Commun. 50 (2014) 7063–7066.
[28] H. Tributsch, Coord. Chem. Rev. 248 (2004) 1511–1530.
[29] L.J. Shen, S.J. Liang, W.M. Wu, R.W. Liang, L. Wu, J. Mater. Chem. A 1 (2013) 11473–11482.
[30] L.J. Shen, W.M. Wu, R.W. Liang, R. Lin, L. Wu, Nanoscale 5 (2013) 9374–9382.
[31] L.J. Shen, S.J. Liang, W.M. Wu, R.W. Liang, L. Wu, Dalton Trans. 42 (2013) 13649–13657.
[32] G. Lu, C.L. Cui, W.N. Zhang, Y.Y. Liu, F.W. Huo, Chem. Asian J. 8 (2013) 69–72.
[33] W. Zhang, J.D. Hong, J.W. Zheng, Z.Y. Huang, J.R. Zhou, R. Xu, J. Am. Chem. Soc. 133 (2011) 20680–20683.
[34] W. Zhang, R. Xu, Int. J. Hydrogen Energy 37 (2012) 17899–17909.
[35] W.J. Luo, Z.S. Li, T. Yu, Z.G. Zou, J. Phys. Chem. C 116 (2012) 5076–5081.